Scattering-matrix approach for a quantitative evaluation of the topological protection in valley photonic crystals

Gaëtan Lévêque [*] and Yan Pennec
Institut d'Electronique, de Micro-électronique et de Nanotechnologie, UMR No. 8520, CNRS,
Université de Lille, Cité Scientifique, Avenue Poincaré, 59652 Villeneuve d'Ascq, France

Pascal Szriftgiser and Alberto Amo
Laboratoire de Physique des Lasers Atomes et Molécules, UMR No. 8523, CNRS, Université de Lille, 59000 Lille, France

Alejandro Martínez
Nanophotonics Technology Center, Universitat Politècnica de València, Camino de Vera s/n, 46022 Valencia, Spain

The realization of photonic crystal waveguides with high topological protection enables robust light propagation against defect-induced scattering. It should allow the design of very compact devices by exploiting guiding through sharp bends with low losses and backreflection. In this work we use valley topological triangular resonators coupled to an input waveguide to evaluate the conversion between helical topological edge modes with opposite helicity at sharp bends or routing elements like splitters. To that purpose, we first analyze via numerical simulations the existence of backward scattering at cavity corners or transmission with helicity conversion at the splitter between the input waveguide and the cavity. We show evidence that such processes take place, in particular at sharp corners, which results in transmission minima and split resonances, otherwise nonexistent. In order to evaluate the small coupling coefficients associated with this effect, a phenomenological model based on an exact parametrization of scattering matrices at splitters and corners of the resonators is then introduced. By comparison with the numerical simulations, we are able to quantify the helicity conversion at sharp bends and splitters. Finally, we use the obtained set of phenomenological parameters to compare the predictions of the model with full numerical simulations for fractal-inspired cavities based on the Sierpiński triangle construction. We show that the agreement is overall good but shows more differences for the cavity composed of the smallest triangles. Our results suggest that even in a system exempt from geometrical and structural defects, helicity conversion is not negligible at corners, sharp bends, and splitters. However, simpler but predictive calculations can be realized with a phenomenological approach, allowing simulations of very large devices beyond the reach of standard numerical methods, which is crucial to the design of photonic devices which gather compactness and low losses through topological conduction of electromagnetic waves.

I. INTRODUCTION

Topological photonics has recently become a disruptive paradigm enabling exotic ways to manipulate light propagation [1–5]. Among the different platforms to implement photonic structures relying on topological effects, two-dimensional (2D) high-index photonic crystal slabs display interesting features such as lossless propagation and large bandwidth, compatible with standard microfabrication tools [6–12]. An interesting proposal to build a topologically protected waveguide in a 2D photonic crystal was presented by Wu and Hu [13]. Essentially, the idea is to design the unit cell of a honeycomb lattice so that it shows a Dirac cone at the Γ point at a given frequency. Then by either shrinking or expanding the motif inside unit cells, a topological band gap arises. The interface between two semi-infinite shrunken

and expanded lattices supports topologically protected modes showing certain pseudospins for given propagation directions [13]. Remarkably, when this approach is applied to 2D photonic crystal slabs, the guided modes are always over the light line, meaning they are always radiative, a property that has been used to identify the pseudospin of the guided modes via far-field measurements [9,10]. The realization of large-scale photonic integrated circuits requires, however, waveguides that do not radiate. In photonic crystal slabs, this means that the guided modes should be below the light line to ensure perfect confinement by total internal reflection. The realization of topological waveguides supporting fully guided modes would require thus a honeycomb lattice or other geometries showing, when undeformed, a Dirac point at symmetry points different from Γ in the first Brillouin zone. In contrast to the shrunken-expanded configuration, which mimics the spin Hall effect for photons, photonic analogs of the valley Hall effect have been proposed [14,15] and experimentally realized [7,8,16]. Since experimental works use standard silicon technology,

———————
*gaetan.leveque@univ-lille.fr

043505-1

valley Hall photonic waveguides show a huge potential to become key elements in silicon photonics. One of the great advantages over light waveguiding along line defects in trivial photonic crystals is the ability, due to the topological protection, to conduct light even along sharp corners, with angles as large as 120° [7,8,17,18]. This would allow for increasing the compacity and decreasing the footprint of future devices for information and communication technologies. However, unlike in other topological photonic systems in which the time-reversal symmetry is broken (for instance, by applying an external magnetic field [19,20]), in photonic crystals the band structure is symmetric with respect to the wave vector in the propagation direction. This means that for any topological guided mode having a certain helicity relying on its valley number and wave vector, there will be an identical state with opposite helicity. In particular, as the valley Chern number, obtained by integration of the Berry curvature on half of the unit cell around K or K' points [21], is not a topological invariant, no bulk-boundary correspondence applies and strict topological protection does not happen [22,23] (except for a certain class of perturbations [24]) in those systems: Although the topology of the system provides certain robustness to the propagation [7,8], helicity conversion is not prohibited by nature. Recently, several groups have evaluated the topological protection in valley photonic crystals. Arora *et al.* [18] made a direct experimental quantification of that protection by probing *in situ* the topological modes along series of sharp bends of zigzag edges in valley photonics crystals made of triangular holes. Protection against random structural imperfections is as well a crucial property, which has been assessed on topological slow light propagation numerically by Arregui *et al.* [25] and experimentally by Rosiek *et al.* [26]. We propose here a quantitative evaluation of the topological protection by evaluating the helicity conversion in *perfect* topological crystals due to corners and other routing elements like splitters. Such a study allows assessing the applicability of those concepts to more complex photonic systems, particularly in the case of ringlike cavities in which the finesse is highly sensitive to the geometry of the circuit due to the continuous recirculation of light.

We analyze via numerical simulations the properties of valley topological edge modes built in 2D photonic crystals. In particular, we focus on the helicity conversion at sharp corners and splitters of triangular resonators coupled to a linear waveguide [27–30], from either a corner or the middle of an edge. In such systems, in the absence of absorption, no resonant features would be expected in the transmission spectra if strong topological protection was realized: Any deviation from a flat transmission band can in principle be traced back to an edge-mode conversion somewhere along the path of light. We show that, in triangular resonators with different coupling conditions, transmission spectra present minima and split resonances essentially due to the coupling between counterpropagating waves within the cavity, as in the case of other nontopological traveling-wave resonators [31]. In order to elucidate and quantify the origin of the phenomenon, we then introduce a phenomenological model relying on the description of corners and splitters by scattering matrices whose exact expressions are derived. The numerical evaluation of the eight real parameters describing those

matrices allows reproducing very precisely the simulations and assessing the small frequency-dependent coupling coefficients corresponding to helicity conversions at corners and splitters. Our results evidence that, even in the case of propagation of light in topological circuits free from geometrical and structural imperfections, reflection at sharp corners dominates the overall shape of transmission spectra, whose finer details are attributed to weaker conversion processes at the splitter. We conclude our study by demonstrating that our phenomenological model allows predictive and faster numerical simulations of complex circuits, giving the example of fractal-inspired resonators based on a Sierpiński triangle construction.

II. NUMERICAL APPROACH

Our topological photonic crystal (TPC) [see Fig. 1(a)] is based on the well-known hexagonal-lattice geometry made of circular holes with radii r_1 and r_2, investigated for example by He *et al.* [8] and in other works [28,29]. The study is restricted to TE (in-plane) polarization. For our bidimensional system, we choose a lattice constant $b_0 = 385$ nm, an average hole radius $r_0 = 130$ nm, and a refractive index $n = 2.7$. Those values allow matching the band gap of the silicon membrane described in Ref. [8]. Unless specified otherwise, all numerical simulations have been performed using the finite-element-method (FEM) software COMSOL MULTIPHYSICS. When $r_1 = r_2 = r_0$, the band diagram of the resulting honeycomb lattice presents Dirac cones at the six K points at the edge of the first Brillouin zone (FBZ), close to $f_0 = 216$ THz [Fig. 1(b), black dashed line]. A band gap is then opened around f_0 for $r_1 \neq r_2$ [Fig. 1(b), blue solid line], where the sixfold rotational symmetry of the lattice point group is lowered to threefold due to the breaking of inversion symmetry. For $r_1 = 180$ nm and $r_2 = 80$ nm, the band gap corresponds to the frequency window [205.7 THz, 220.7 THz], indicated by the gray area.

The bands surrounding this band gap present a nontrivial local topology, as expected from the valley Hall effect. This can be readily seen by computing the Berry curvature of those bands using a plane-wave expansion method [21] (see details in Appendix A). Figure 1(c) shows the calculated Berry curvature for the first band (top diagram) and for the ensemble of bands 2 and 3 (bottom diagram), which are touching. In both cases, the Berry curvature is concentrated at the K and K' points. For a given band, it has opposite sign at K and K', as expected for a time-reversal symmetric system, and at a given K or K' point, each set of bands presents Berry curvatures of opposite sign. This configuration of opposite signs at opposite K and K' points and different bands is at the origin of the interface topological modes when two mirror-symmetric photonic crystals are pasted together. This is confirmed by the nonzero values of valley Chern numbers, calculated by integrating the Berry curvature around the K and K' points: We obtain ∓ 0.090 for the first band and ± 0.076 for the second and third bands. The computed Chern numbers are low compared to the usually expected values of $\pm 1/2$. Actually, as mentioned by several authors [8,32], the Chern number is a half-integer in the limit of weak perturbations, which corresponds here to small asymmetries of the holes'
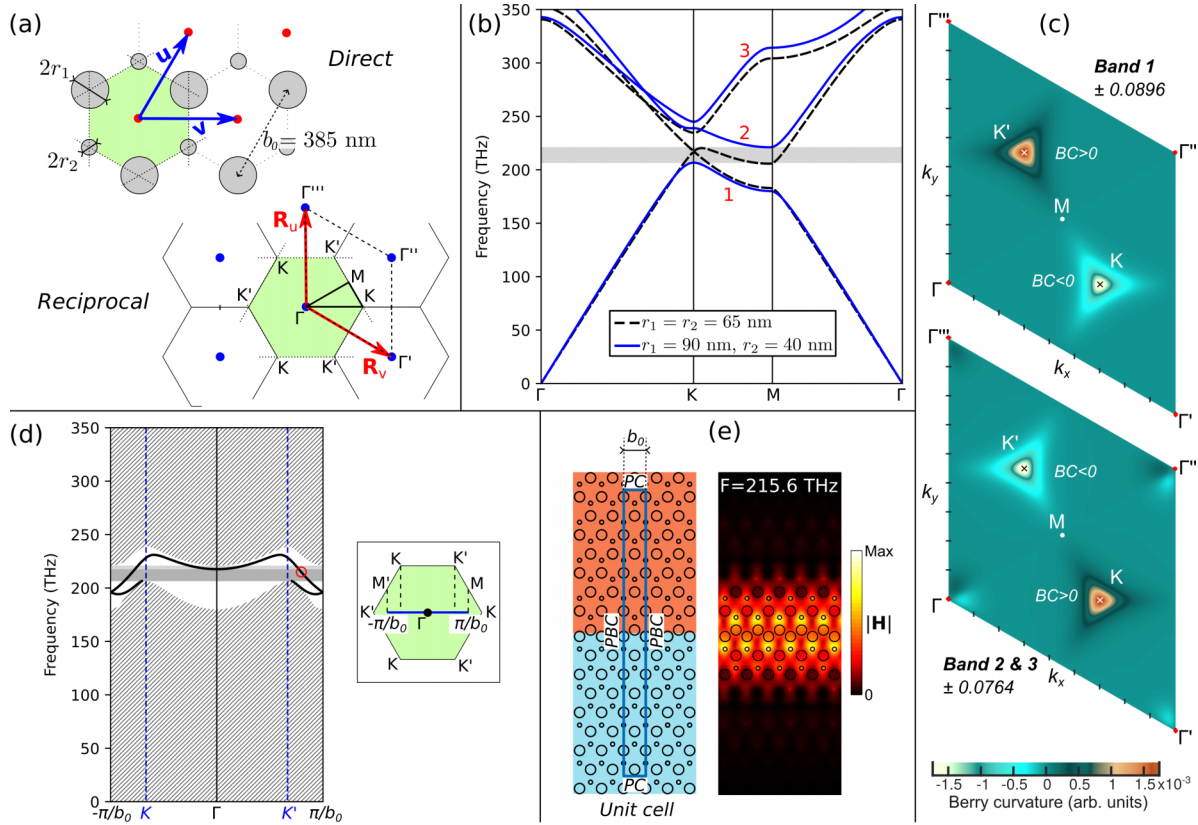
FIG. 1. (a) Geometry of the TPC and representation of the reciprocal space and associated high-symmetry points. (b) Dispersion diagram of the TPC for equal (black dashed line) or different (blue solid line) radii r_1 and r_2 of the two holes inside each primitive cell. (c) Berry curvature (BC) and valley Chern numbers simulated for the disymmetric TPC ($r_1 = 180$ nm and $r_2 = 80$ nm), where the top and bottom diagrams correspond to the first band and to the degenerated second and third bands, respectively. The sign of the Berry curvature is indicated next to each corresponding K and K' point. (d) Dispersion curves (black solid lines) of the edge modes propagating along the bearded interface in between two semi-infinite mirror-symmetric TPCs, parallel to the ΓK direction (the gray hatched background indicates the projected bulk modes). The inset compares the FBZ of the interface (blue solid line with length $2\pi/b_0$) and the FBZ of the infinite TPC. (e) Shown on the left is a typical unit cell used in the simulation, limited by periodic boundary conditions (PBC) [a perfect conductor (PC)] along the vertical (horizontal) boundaries of the blue rectangle. Shown on the right is the distribution of the magnetic-field amplitude of the edge mode for a frequency of 215.6 THz, indicated by the red circles on the dispersion curve.

radii. In order to open an appreciable band gap, r_1 must be significantly different from r_2, which leads to an overlap of the Berry curvatures with opposite signs in each half of the. FBZ, finally resulting in lower Chern numbers [8].

We show in Fig. 1(d) the dispersion relation of the topological edge mode propagating along a bearded ΓK edge, in between two semi-infinite TPCs with glide mirror symmetry [in orange (top TPC) and blue (bottom TPC) in Fig. 1(e)]. The system being now uni-dimensional with period b_0, its FBZ is a segment with length $2\pi/b_0$ in the ΓK direction (see the inset), fully included inside the FBZ of the TPC. The breakdown of periodicity in the direction perpendicular to the edge direction induces a projection of the bulk modes of the infinite TPC onto the linear FBZ, which correspond to the hatched gray background, and of K and K' points onto the points indicated by the blue dashed lines. The dispersion curve has been simulated using a supercell approach, for which a typical rectangular shape is plotted in Fig. 1(e) on the left. Periodic boundary conditions have been applied along the vertical edges of the supercell, while perfect conductors have been used for the two edges parallel to the interface. The length of the rectangle has

been taken long enough to ensure that the edge mode has a negligible amplitude along the top and bottom boundaries. The distribution of the magnetic-field amplitude of the edge mode for a frequency of 215.6 THz is plotted in Fig. 1(e) on the right: The field is concentrated at the interface between the two crystals with a penetration length of about 1.5 unit cells into the bulk. The dispersion curve of the topological mode reaches a local minimum at the Γ point, with a frequency of about 217.1 THz, lower than the bottom of the bulk band gap. For that reason, the effective band gap for the topological edge mode is [205.7 THz, 217.1 THz], underlined in dark gray in Fig. 1(d). From this simulation, we can extract the evolution of the wave vector or, equivalently, the effective index of the topological edge mode with frequency.

III. TRIANGULAR RESONATORS

To investigate the robustness of the topological protection, we now characterize the properties of triangular edge mode resonators coupled to waveguides built on ΓK bearded edges. Such cavities can be coupled to a waveguide in two

different ways, either from the edge [Fig. 2(a)] or from the corner [Fig. 2(b)]. In both situations, the injection of the topological mode inside the resonator is realized through a splitter with four branches and labeled by S, while the corners of a triangular cavity will be denoted by C. As shown in Figs. 2(a) and 2(b), if no helicity conversion occurs in the system (which means at S and C points), all topological modes propagate along each edge with the same helicity and then in the same direction. As a consequence, the system cannot reflect waves in the excitation guide, which means that the reflection coefficient R in power is zero, and through energy conservation the transmission coefficient T in power is unity. Even if resonances in amplitude can occur inside the triangular cavity, they cannot have a signature in the transmission or the reflection spectra.

The numerical simulations (see Appendix B) of triangular cavities with edge length $L \approx 28b_0$ are presented in Figs. 2(c)–2(f). The TPC containing the resonators and the coupling guide is surrounded by perfectly matched layers (PMLs), whose role is to absorb the field along the outer edge of the simulation domain to simulate an infinite system. The transmission is computed by integrating the Poynting vector's flux across a line perpendicular to the output waveguide, whose length is long enough to capture all the power carried by the transmitted edge mode (see Fig. 10 in Appendix B). The normalized transmission T is then obtained after normalization of the transmission by the power flowing along a straight waveguide without a resonator, computed in a similar way. Additionally, $1 - R$, where R is the normalized reflection, is computed with the same method but by integration along a line perpendicular to the input waveguide (see Fig. 10 in Appendix B). The spectra show, in contrast to the previous analysis, narrow transmission dips regularly separated in frequency, for both edge- and corner-addressed resonators, however with different profiles and frequencies. The simulation domain is taken large enough to minimize the coupling of evanescent fields emanating from the structures (for example, corners) with PMLs: We can then verify numerically that $T \approx 1 - R$, as black solid (T) and green dashed ($1 - R$) curves overlap in the band gap. In order to fully explain the transmission and reflection spectra, we need to suppose the existence of processes of helicity conversion in the system. For that reason, the topological edge mode can travel in the directions corresponding to the same helicity as for the excitation mode [blue arrows in Figs. 2(d) and 2(f)] or the opposite helicity indicated by the red arrows. Conversions can originate from the splitter or the triangle corners.

Both spectra present split resonances with low transmission ($T \approx 0$, two and four for the edge- and corner-addressed resonators inside the effective gap, respectively) and profiles characterized by a quasiunity transmission ($T \approx 1$, three and one, respectively) in between two transmission minima above 0.5 in power, called antiresonances below. Split resonances can be related to mode splitting arising from backscattering in standard ring resonators [31,33]. Typical distributions of the magnetic-field amplitude are presented in Figs. 2(d) and 2(f) for split resonances and antiresonances. For both transmission minima of the split resonance at $F \approx 209$ THz (edge-addressed cavity), a clear interference pattern is obtained inside the cavity and in the excitation guide. The
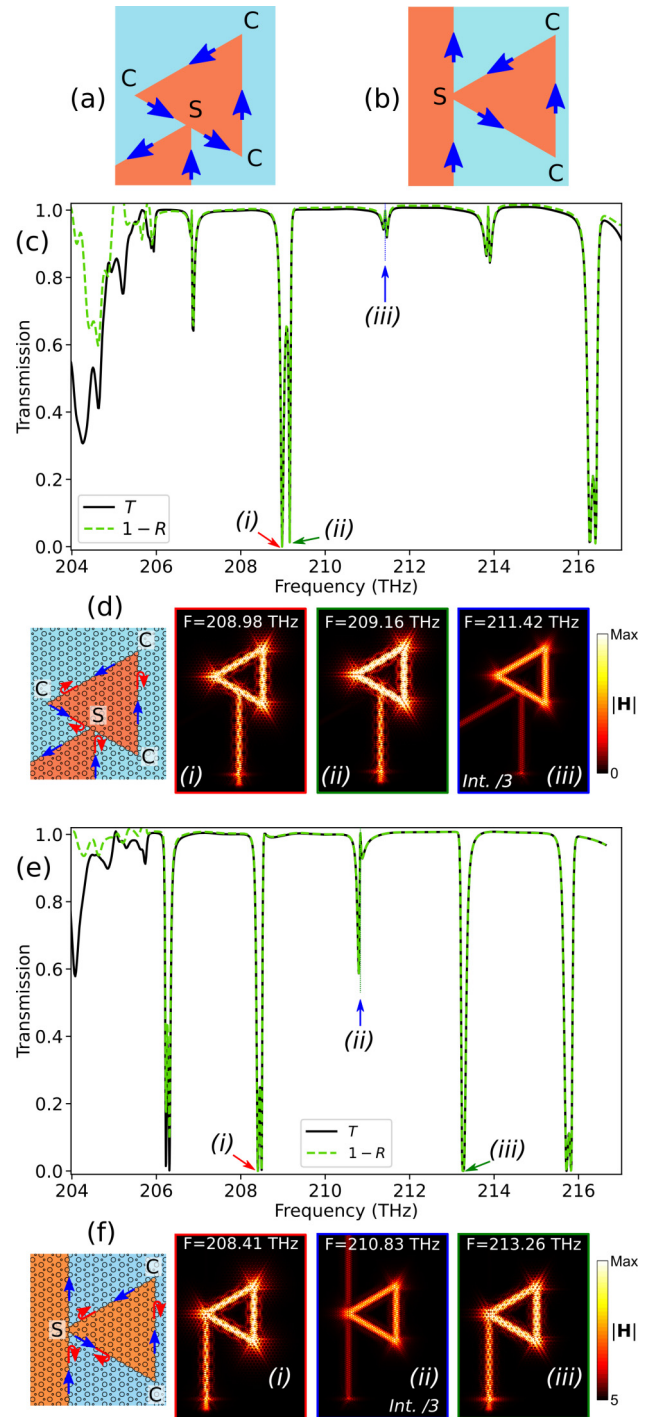

FIG. 2. Representations of (a) an edge-addressed and (b) a corner-addressed topological triangular cavity. Blue (dark gray) arrows indicate the helicity of the input edge mode. (c) Comparison between T (normalized transmission, black solid line) and $1 - R$ [green (gray) dashed line, where R is the normalized reflection] spectra obtained from numerical simulations for the edge-addressed cavity. (d) Shown on the left is a schematic indicating with red (lighter gray) arrows the edge modes with helicity opposite to the input edge mode. Shown on the right are distributions of the magnetic-field amplitude for frequencies indicated by a colored arrow [and labeled (i)–(iii)] in (c). For $F = 211.42$ THz, the maximum value is three times larger than for the two first frequencies. (e) and (f) Same as in (c) and (d) but for the corner-addressed cavity.

difference between both distributions is visible along the bisector plane crossing each corner: Along those planes, the magnetic field is maximum or minimum for the lowest and highest frequencies, respectively. The frequency difference is about 160 GHz and the full width at half maximum (FWHM) is 100 and 50 GHz, corresponding to quality factors of $Q = 2090$ and 4180, respectively. At the antiresonance ($F \approx 211$ THz, blue arrow), the transmission is close to unity and no interference pattern is observed accordingly in the coupling waveguide, but a small intensity modulation is visible along the triangular cavity. Notice that the color scale is the same for all distributions, except for the antiresonances where the maximum value of the magnetic-field amplitude is three times higher. Similar observations can be made on the field distributions of the corner-addressed cavity [see Fig. 2(f)]: The shape of the input waveguide does not modify the field distribution at the split resonances or antiresonances, despite their frequency shift compared to the corner-addressed cavity.

If the occurrence of transmission split resonances and antiresonances is a signature of a conversion between edge modes with opposite helicities, it is difficult from the numerical simulation to quantify this phenomenon and find its origin. To this purpose, we propose in the next section a phenomenological approach where both the splitter and triangle corners are described by a scattering matrix, allowing a simplified description of the systems.

IV. PHENOMENOLOGICAL MODEL

Our phenomenological model of the triangular resonators relies on the description of the splitter S and corners C by a scattering matrix, which expresses a linear relation between outgoing waves with amplitudes $A^-, B^-, C^-, \ldots$ and incoming waves with amplitudes $A^+, B^+, C^+, \ldots$ (see Fig. 3). The matrix elements can be partly extracted from numerical simulations. The topological nature of those modes implies that several of those elements are expected to be zero or much smaller than unity. The details of the calculations are given in Appendix C, but we outline the main results below.

A simple corner, in the most general situation, behaves like a coupler between the two incident edge modes described by the complex vector $\mathbf{X}^+ = [A^+, B^+]^T$ with the corresponding transmitted and backscattered modes $\mathbf{X}^- = [A^-, B^-]^T$ [see Fig. 3(a)]. The shape of the scattering matrix, defined by the relation $\mathbf{X}^- = \mathbf{M}_C \mathbf{X}^+$, is constrained by energy conservation, which implies that $\mathbf{M}_C$ is unitary, and time-reversal symmetry, which, combined with unitarity, implies that $t_1 = t_2$. Finally, $\mathbf{M}_C$ has the following general form:

$$\mathbf{M}_C = \begin{bmatrix} t_1 & r_1 \\ r_2 & t_2 \end{bmatrix} = e^{i\tau} \begin{bmatrix} \cos\sigma & i\sin\sigma \\ i\sin\sigma & \cos\sigma \end{bmatrix}.$$

The phase τ and angle σ can take arbitrary values. For convenience, we note in the following that $a = t_1 = t_2$ and $b = r_1 = r_2$.
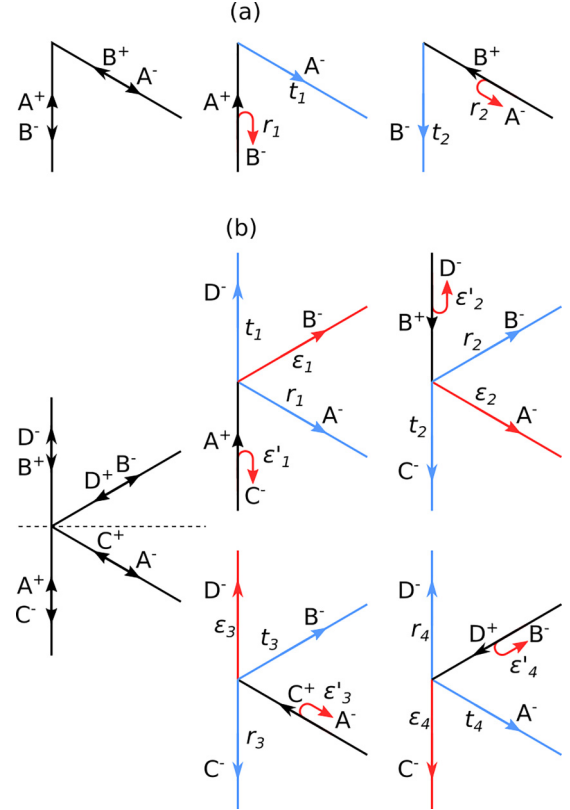

FIG. 3. Definition of the coupling coefficients and edge-mode amplitudes as employed in the scattering-matrix phenomenological model. (a) For the corner, input (A^+, B^+) and output (A^-, B^-) amplitudes are defined in the left panel. Scattering coefficients $r_{1,2}$ and $t_{1,2}$ are defined in the middle and right panels, respectively for excitation in the A^+ direction ($B^+ = 0$) and in the B^+ direction ($A^+ = 0$). (b) For the splitter, the input amplitudes are labeled A^+, B^+, C^+, and D^+ while the output amplitudes are labeled A^-, B^-, C^-, and D^- (left panel). Similarly to the corner, the four other panels allow defining the four scattering coefficients $r_{1,2,3,4}$, $t_{1,2,3,4}$, $\epsilon_{1,2,3,4}$, and $\epsilon'_{1,2,3,4}$ related to each direction of the input wave. The blue (light gray) lines indicate the directions conserving the helicity of the excitation, while the red (dark gray) lines correspond to the helicity conversion.

Concerning the splitter, four outputs $\mathbf{X}^+ = [A^+, B^+, C^+, D^+]^T$ are now connected via the scattering matrix $\mathbf{M}_S$ to four inputs $\mathbf{X}^- = [A^-, B^-, C^-, D^-]^T$ [see Fig. 3(b)], with *a priori* 16 complex coefficients defined in the figures. However, the symmetry of the system implies that $\alpha_1 = \alpha_2$ and $\alpha_3 = \alpha_4$, where $\alpha = r, t, \epsilon, \epsilon'$, and we will note that $t_1 = t_2 = t$, $t_3 = t_4 = t'$, $\epsilon'_1 = \epsilon'_2 = \epsilon'$, and $\epsilon'_3 = \epsilon'_4 = \epsilon''$. Energy conservation implies the unitarity of $\mathbf{M}_S$, and time-reversal symmetry allows showing that all the r_i and ϵ_i coefficients are equal. Finally, additional symmetry considerations on the geometry of the splitter lead to the

parametrization of $\mathbf{M}_S$,

$$
\mathbf{M}_S = \begin{bmatrix} r & \epsilon & \epsilon'' & t' \\ \epsilon & r & t' & \epsilon'' \\ \epsilon' & t & r & \epsilon \\ t & \epsilon' & \epsilon & r \end{bmatrix}
$$

$$
= \frac{e^{i\alpha}}{2} \begin{bmatrix} c_\phi e^{i\rho} + c_{\phi'} e^{-i\rho} & c_\phi e^{i\rho} - c_{\phi'} e^{-i\rho} & i(s_\phi e^{-i\delta} - s_{\phi'} e^{i\delta})e^{-i\beta} & i(s_\phi e^{-i\delta} + s_{\phi'} e^{i\delta})e^{-i\beta} \\ c_\phi e^{i\rho} - c_{\phi'} e^{-i\rho} & c_\phi e^{i\rho} + c_{\phi'} e^{-i\rho} & i(s_\phi e^{-i\delta} + s_{\phi'} e^{i\delta})e^{-i\beta} & i(s_\phi e^{-i\delta} - s_{\phi'} e^{i\delta})e^{-i\beta} \\ i(s_\phi e^{-i\gamma} - s_{\phi'} e^{i\gamma})e^{i\beta} & i(s_\phi e^{-i\gamma} + s_{\phi'} e^{i\gamma})e^{i\beta} & c_\phi e^{i\rho} + c_{\phi'} e^{-i\rho} & c_\phi e^{i\rho} - c_{\phi'} e^{-i\rho} \\ i(s_\phi e^{-i\gamma} + s_{\phi'} e^{i\gamma})e^{i\beta} & i(s_\phi e^{-i\gamma} - s_{\phi'} e^{i\gamma})e^{i\beta} & c_\phi e^{i\rho} - c_{\phi'} e^{-i\rho} & c_\phi e^{i\rho} + c_{\phi'} e^{-i\rho} \end{bmatrix}, \quad (1)
$$

with the additional constraint $\gamma + \delta + 2\rho = 0$ and the definitions $c_x = \cos x$ and $s_x = \sin x$. The $\mathbf{M}_S$ matrix is then parameterized by six free parameters: The two angles ϕ and ϕ' and the four phases α, β, γ, and δ.

We now need to numerically evaluate eight real parameters: Two for $\mathbf{M}_C$ and six for $\mathbf{M}_S$. To that purpose, reference points have to be defined in order to evaluate the phases of the matrices coefficients. Concerning the corner, the reference is taken as the intersection of the average lines of the bearded edges, as shown in Fig. 4(a). The transmission, $a = \exp(i\tau)\cos\sigma$, and reflection, $b = i\exp(i\tau)\sin\sigma$, coefficients have been numerically evaluated simulating the propagation of the edge mode along a single corner, whose magnetic-field amplitude distribution is shown in Fig. 4(b). The phase $\phi_a = \tau$ of the transmission coefficient a is obtained by comparing the phase of the transmitted mode to the phase of a mode propagating along a straight waveguide (see Appendix D). The numerical phase and a second-order polynomial fit are plotted in Fig. 4(c). The amplitude $|b|$ of the reflection coefficient is directly given by the contrast of the interference pattern in the injection guide, which is observable, despite being weak, on

the magnetic-field distribution of Fig. 4(b). Figure 4(d) shows the contrast as a function of the frequency, which presents a noticeable oscillation due to the interference with the wave which is slightly backscattered on the PML. However, we can obtain a correct approximation of $|b|$ by evaluating the average contrast, on the order of 8–9 % in amplitude. As $\phi_b = \phi_a + \pi/2$ and $|a| = \sqrt{1 - |b|^2}$, the matrix $\mathbf{M}_C$ is fully determined, within the simulation uncertainties.

For the splitter, we have evaluated both the amplitudes and phases of the reflection (r) and transmission (t and t') coefficients defined in the phenomenological model [see Eq. (1)]. As indicated in Fig. 5(a), the four-branch splitter can be addressed either from one of the oblique branches (left panel) or from one of the vertical (right panel) branches. Following the definition of the coupling coefficients and taking the example of the oblique excitation, the wave can be transmitted with a coefficient t' to the second oblique branch (called the transmission branch), reflected with a coefficient r into a topological mode with the same helicity propagating along the downward vertical branch (reflection branch), coupled to a mode with opposite helicity with a coefficient ϵ propagating along the upward vertical branch (forbidden branch), or backscattered into the mode with opposite helicity into the excitation branch with coefficient ϵ''. Similarly in the second case and with equivalent denomination, the wave coming from a vertical branch can be coupled to the transmission branch t, the reflection branch (downward oblique branch r), the forbidden branch (upward branch ϵ), or backscattered (ϵ'). As shown above, the coefficients r and ϵ must be the same in both cases (excitation from a vertical or an oblique branch), but the transmission and backscattering coefficients can be different. The evolutions with frequency of the squared modulus of the transmission, reflection, and forbidden transmission coefficients are plotted in Fig. 5(b), with solid lines for the vertical excitation and with colored pluses for the oblique excitation. First, we can verify that the transmission and the reflection coefficients have nearly equal values in both configurations. Second, it appears clearly that the coefficient ϵ is weak (see the green solid line). For this reason, it cannot be evaluated by this method because the average value, below 1% in intensity, could be related to the reflection of the transmitted and reflected waves on the PMLs surrounding the simulation domain. As a consequence, $|\epsilon|^2$ can have any value between 0% and about 1%. As numerically $|t|^2 + |r|^2 \approx 1$, ϵ' and ϵ'' are confirmed to be, as ϵ, much smaller than 1.
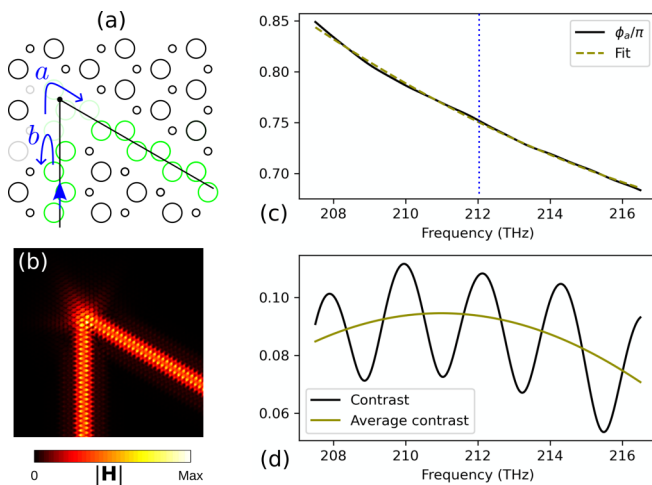

FIG. 4. (a) Transmission (a) and reflection (b) coefficients on a corner. (b) Distribution of the magnetic-field amplitude at $F = 212$ THz. (c) Transmission phase ϕ_a normalized to π computed from numerical simulations. (d) Contrast of the interference pattern along the vertical input edge in (a) (black solid line) and average contrast [olive (gray) line].
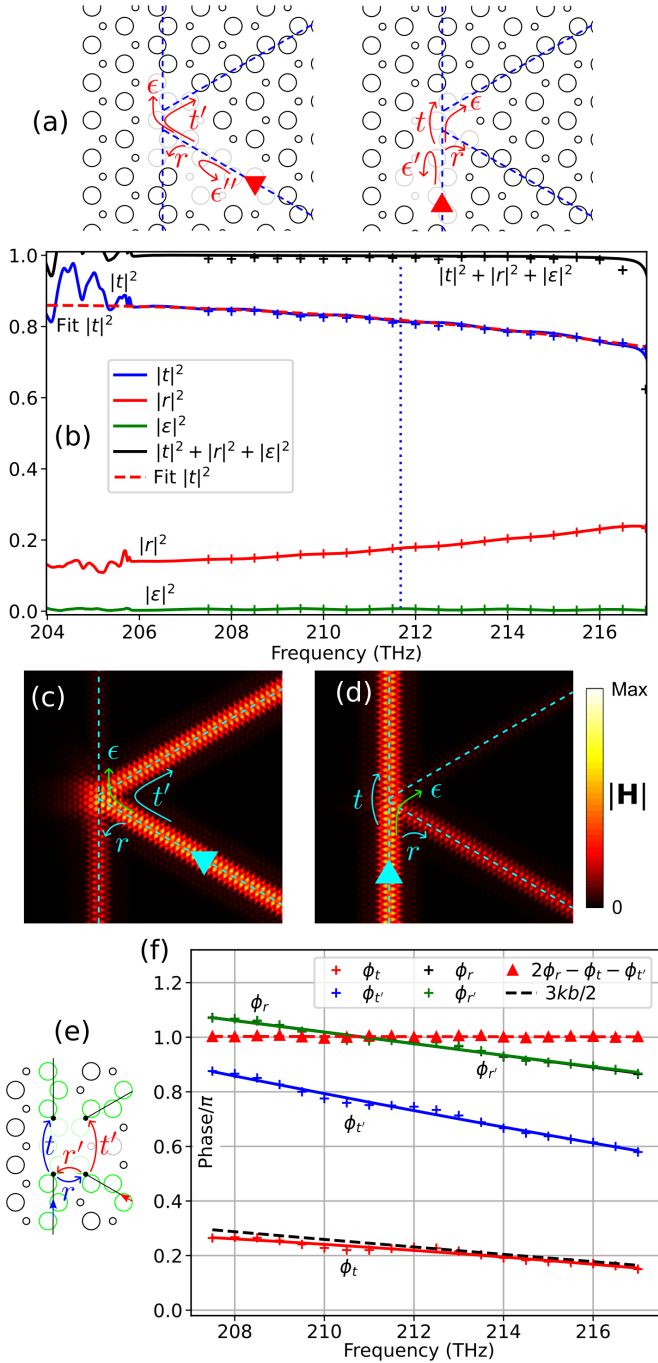
FIG. 5. (a) Geometry of the splitter and coupling coefficients when addressed from an oblique (left) or a vertical (right) branch. (b) Evolution of the intensity of the waves propagating along each branch of the splitter. Solid lines (pluses) correspond to the illumination along the vertical (oblique) branch. The distribution of the magnetic-field amplitude is plotted for (c) oblique and (d) vertical incidence. (e) Transmission and reflection coefficients across the splitter for vertical (t, r) and oblique (t', r') incidence. (f) Phases of the different coefficients across the splitter.

In that case, as the coefficient r is supposed to be the same in oblique or vertical excitation, energy conservation implies that $|t| \approx |t'|$, which is correctly reproduced by the numerical simulation. This tends to show that topological protection is

quite robust at the splitter. The dashed line is a second-order fit of $|r|^2$, which varies between 84% and 76%. The distribution of the magnetic-field amplitude is plotted in Figs. 5(c) and 5(d) for oblique and vertical excitation, respectively, at a frequency of 212 THz. We can visually verify the equality of the transmission and reflection coefficients. A very faint field can be distinguished along the forbidden channel, which may be again attributed to weak reflection of the transmitted and reflected fields on PMLs. As a conclusion, it is reasonable to consider as a first approximation that the routing of edge modes through the splitter preserves helicity: An incident topological mode can be coupled to either the transmission channel (with coefficients t of t') or the reflection channel (with coefficient r) but not to the forbidden channel ($\epsilon = 0$); nor can it be backreflected ($\epsilon' = \epsilon'' = 0$). Those results agree well with those obtained by Ma *et al.* [17] for a similar splitter but with triangular holes. In Eq. (1) it appears that conservation of helicity corresponds to $\phi = \phi'$ and $\gamma = \delta = 0$, which we suppose in the next paragraph.

In order to evaluate the phases of t, t', and r, reference points have been defined as indicated in Fig. 5(e): The phase will be for each coefficient the phase difference of the topological mode between two points linked by the corresponding arrow. Figure 5(f) shows the frequency evolution of the four phases ϕ_t, $\phi_{t'}$, ϕ_r, and $\phi_{r'}$, normalized to π, corresponding to coefficients t, t', r, and r'. We can first verify numerically that, as predicted by energy conservation and time-inversion symmetry, $\phi_r = \phi_{r'}$ and finally $r = r'$. The second point is that the phase ϕ_t for the transmission coefficient along the straight edge of the connection is equal, within the numerical uncertainties, to the propagation phase of the wave along the distance $3b_0/2$ between the two reference points of t. No additional phase is introduced by the presence of the nearby oblique edges. Next the three phases ϕ_t, $\phi_{t'}$, and ϕ_r are related to α and β ($\gamma = \rho = 0$) through

$$\alpha + \beta + \pi/2 = \phi_t,$$
$$\alpha - \beta + \pi/2 = \phi_{t'},$$
$$\alpha = \phi_r,$$

which leads to $\pi[2\pi] = 2\phi_r - \phi_t - \phi_{t'}$. We can see in Fig. 4(f) that this relation is very well verified numerically. As we suppose for now that the splitter preserves helicity, the three remaining coefficients ϵ, ϵ', and ϵ'' are zero.

V. COMPARISON WITH FEM SIMULATIONS

The semianalytical modelization of the triangular resonators is realized using a coupled-wave approach, whose details are given in Appendix E. The principle is summarized in Fig. 14, which shows how C and S points are connected through segments of different lengths. Due to the choice of reference points for the splitter, the lengths of the different triangle edges are slightly different ($L_0 = 28.5b_0$, $L_1 = 27b_0$, and $L_2 = 13.5b_0$). The method relies on the evaluation of a coupling matrix $\mathbf{C}$, which describes how the output fields rely on the input fields through the scattering matrices $\mathbf{M}_C$ and $\mathbf{M}_S$, and the phase matrix $\mathbf{P}$, which gathers the phase accumulation of the topological mode along each edge of the resonators.
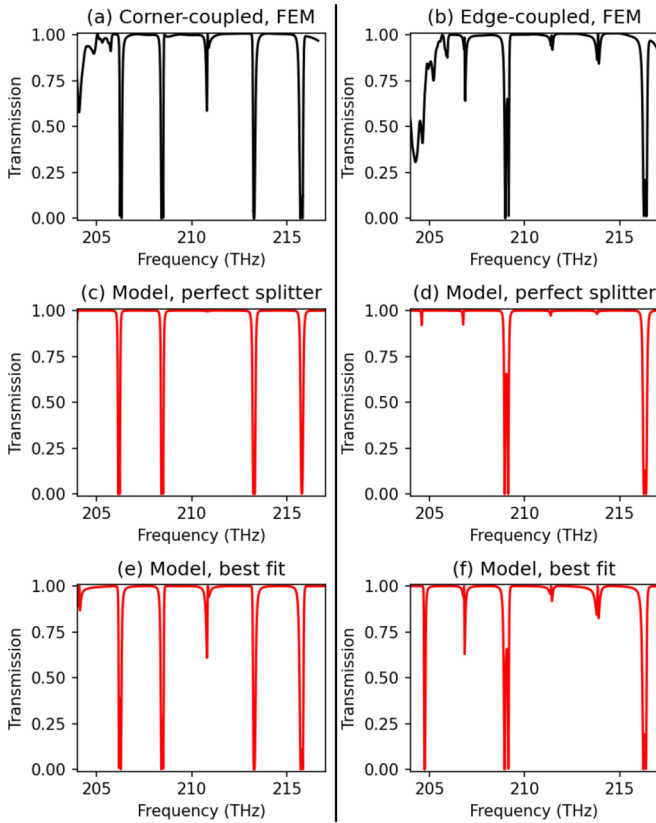
FIG. 6. Comparison between the transmission spectra obtained from finite-element simulations and the phenomenological model for (a), (c), and (e), corner-addressed and (b), (d), and (f), edge-addressed cavities. The splitter is supposed to either (c) and (d) perfectly conserve or (e) and (f) not conserve edge-mode helicity.

FIG. 7. Frequency evolution of the coefficient amplitudes associated with $\mathbf{M}_C$ and $\mathbf{M}_S$ after optimization.

After numerical resolution of Eq. (E1) in Appendix E, the amplitudes of the reflected and transmitted fields are retrieved.

The transmission spectra can be computed for triangular resonators addressed from either the corner or the edge. For the resonators of Fig. 2, the spectra obtained by FEM simulations [Figs. 6(a) and 6(b)] compare very well with the phenomenological model (bottom red lines) even if the splitter is supposed to perfectly preserve helicity [Figs. 6(c) and 6(d)]. Note that a slight adjustment of the edge mode wave vector (by 0.06%) has been realized to have slightly better agreement of the resonance frequencies. The frequencies and alternation of the split resonances ($T = 0$) and antiresonances ($T = 1$) are well reproduced for both corner- or edge-addressed resonators, and the FWHM are comparable. The main difference is the profiles close to the antiresonances, which are barely visible in Figs. 6(c) and 6(d) but are much more pronounced in the numerical simulation, with a strong asymmetry. This fact then has to be related to helicity conversion at the splitter. Despite the fact that the parameter space of the system is large, with eight free real parameters, it is possible to adjust the remaining small coefficients (ϵ, ϵ', and ϵ'') by fitting each resonance profile in a narrow frequency region around them. This method allows reaching much better agreement, as shown in Figs. 6(e) and 6(f). Indeed, all the missing features are now recovered, concerning asymmetry of the split resonances and
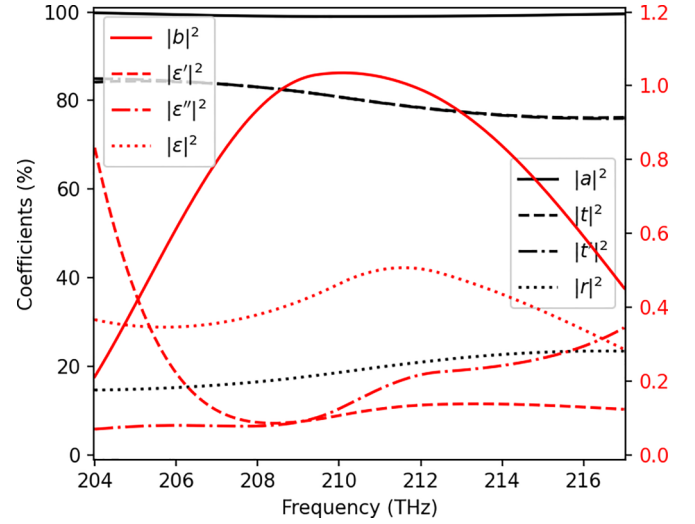
the exact profile of the antiresonances. Figure 7 shows the estimated frequency evolution of the squared amplitude of the eight coefficients corresponding to the corner and splitter scattering matrices. As supposed, the largest coefficient at the origin of the helicity conversion is b, the reflection on a corner, but the coefficients ϵ, ϵ', and ϵ'' are finally comparable. For example, at $F = 212$ GHz, we have $|a|^2 = 0.99$ and $|b|^2 = 0.01$ for the corner and $|t|^2 = 0.784$, $|t'|^2 = 0.783$, $|r|^2 = 0.209$, $|\epsilon|^2 = 5.\,10^{-3}$, $|\epsilon'|^2 = 1.3\,10^{-3}$, and $|\epsilon''|^2 = 2.2\,10^{-3}$ for the splitter. Hence, the helicity conversion is evaluated to be more than two times higher in power at the sharp corners of the triangular resonator (backscattering) than through the splitter (backscattering and forbidden transmission).

As a last study we propose to assess the robustness of the phenomenological approach by comparisons with full numerical simulations of larger and more complex resonators. They consist in three fractal-inspired structures based on the Sierpiński triangle construction, presented in Fig. 8. The first structure [Fig. 8(a)] is simply a corner-addressed triangle whose edges have a length of 51 periods. The second [Fig. 8(b)] is the first iteration of the Sierpiński construction and is composed of four triangles with an edge length of 26 periods. The last resonator [Fig. 8(c)] is the second iteration and is an assembly of one triangle with 26-period-long edges and 12 triangles with 13-period-long edges. The semianalytical simulation is performed in a similar way as explained at the beginning of this section and following the methodology detailed in Appendix E. The size of the problem is however larger, and the dimension of the coupling $\mathbf{C}$ and phase $\mathbf{P}$ matrices reaches 20×20 for the first iteration and 56×56 for the second. The transmission spectrum of the simple triangle has the same general shape as for the resonator previously discussed and shows a similar regular alternation of split resonances and antiresonances, however separated by a smaller frequency interval as the cavity is larger. The comparison between the finite-element simulation [Fig. 8(d)] and the phenomenological model [Fig. 8(g)] again shows very good agreement. For the second structure, more
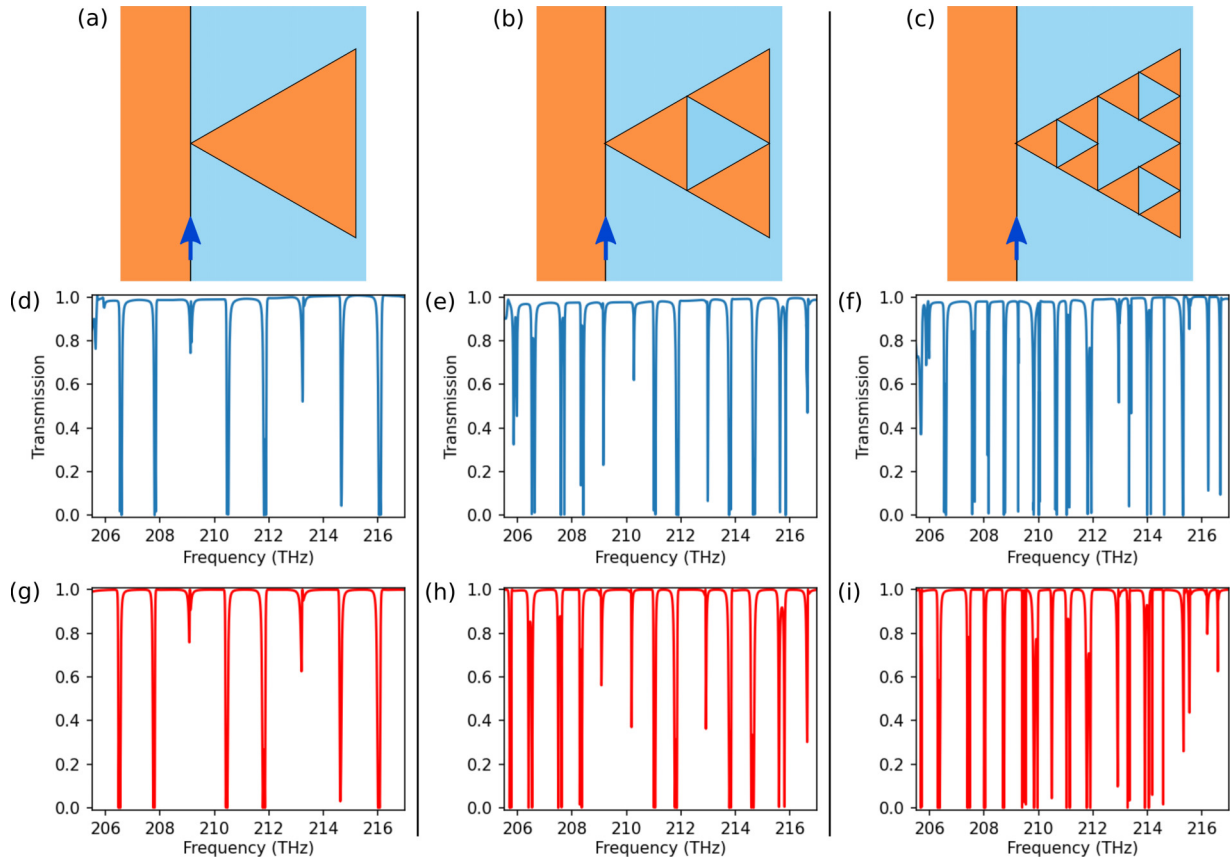
FIG. 8. (a)–(c) Comparison between the full numerical simulation and the phenomenological model for the first three iterations of the Sierpiński triangle construction. (d)–(f) Corresponding transmission spectra computed with the finite-element method. (g)–(i) Transmission spectra calculated with the phenomenological model.

interference paths are possible in the resonator: The simulated transmission spectrum is richer and does not present the same regular pattern obtained for the simple triangle [Fig. 8(e)]. However, the agreement with the phenomenological model is still good [Fig. 8(h)]: Single and split resonances are recovered at the same frequencies, but small differences in amplitude are observed for shallower resonances, close to 209, 210, 213, and 217 THz. The phenomenological model starts to differ more significantly from the numerical simulations for the second iteration. The numerical transmission [Fig. 8(f)] presents consistently more resonances, single or split in two or more peaks. It appears that the number, positions, and amplitudes of those resonances do not coincide as correctly with the phenomenological model, even if some similarities are observed, for example, in term of the density of resonances as a function of the frequency [Fig. 8(i)]. Two main explanations can be proposed. First, as the interference paths are more complex, small errors in the estimations of the matrix coefficients have more significant impact on the transmission. Second, as the edges are shorter, we can expect that the model becomes less valid, as the edge mode, which has a lateral extent, can directly tunnel laterally to adjacent edges across the lattice. An example of the field distribution is shown in Fig. 9 for the resonance at $F = 214.61$ GHz. Despite those limits, our results are encouraging and show that such a phenomenological approach can be employed to

predict, with low computer resources, the propagation of the electromagnetic signal along a complex and extended topological circuit.
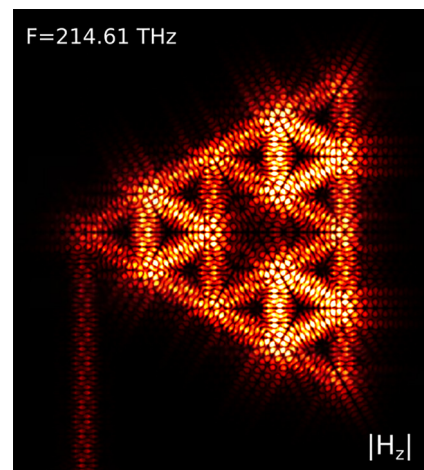

FIG. 9. Distribution of the amplitude of the magnetic field at a resonance of the resonator corresponding to the second iteration of the Sierpiński triangle construction.

VI. CONCLUSION

In this work we have investigated, using a full numerical approach based on the finite-element method and a phenomenological model relying on an exact parametrization of scattering matrices at splitters and corners, the processes of helicity conversion evidenced by the resonance properties of valley topological triangular resonators. In resonators, ideal perfectly robust topological protection would imply a flat transmission band; then any resonance feature must result from a backscattering or forbidden transmission between waves with opposite helicity occurring at particular points of the system (corners, splitters, etc.). In our system, we have demonstrated that the split resonances, together with antiresonances, must be mainly attributed to backscattering at corners of the triangular cavity with a lower but comparable contribution of the splitter. Quantitatively, for the valley topological crystal considered, the amount of power backscattered at corners is about 1% of the incident edge mode, while the backscattering and forbidden transmission at the splitter is lower than 0.5%. We have demonstrated, by simulations of fractal-inspired larger resonators, that our phenomenological approach can be employed for fast and reliable predictive simulations of larger and more complex topological systems, if however the lengths of the edges composing the circuit are not too short (larger than 13 periods in our study) in order to avoid unwanted tunneling between close edges through the photonic lattice. We believe that the proposed methodology can be applied to different geometries of topological photonic devices in order to evaluate the robustness of the topological protection depending on the shape (triangular vs circular) of air holes, edges (bearded or zigzag holes), or configuration of splitters (four or six branches) and corners, which is a crucial point in order to design photonic devices which gather compactness and low losses made possible through topological conduction of electromagnetic waves.

APPENDIX A: BERRY CURVATURE SIMULATIONS

In order to evaluate the Berry phase, the first Brillouin zone is discretized into a 70×70 grid matching the FBZ geometry (not shown here). With MATLAB, due to the plane-wave expansion method, the periodic part of the H_z field component is evaluated over each vertex of the grid. The Berry curvature is reconstructed by computing the accumulated phase around the closed loop made of consecutive points of the discretized grid (see Ref. [21] for more details). Since the first band is isolated from all other bands, its Berry curvature can be computed on its own [Fig. 1(c), top]. Next, by integrating the Berry curvature inside the triangle delimited by points Γ, Γ', and Γ'', on the one hand, and points Γ, Γ'', and Γ''', on the other hand, one can recover the valley Chern numbers associated
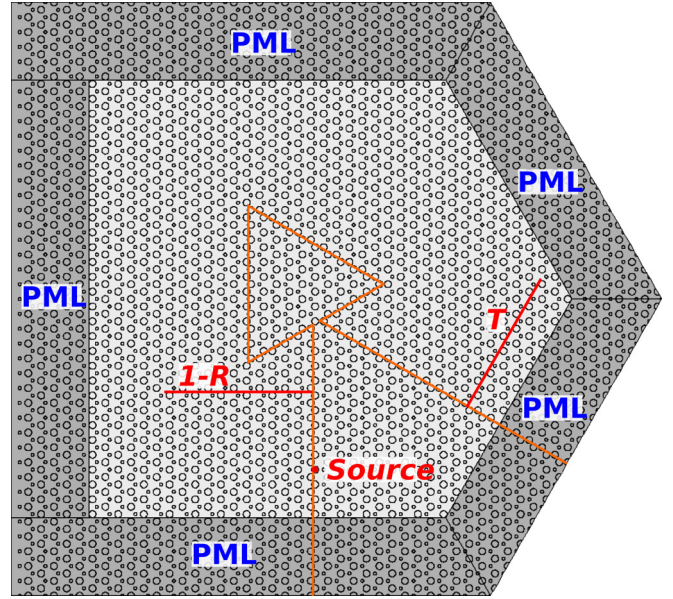
FIG. 10. COMSOL configuration.

with the first band, i.e., -0.090 and $+0.090$. However, bands 2 and 3 are degenerated, i.e., they share identical frequencies at the same location [Fig. 1(c), bottom]. They are however isolated from all other bands. The Berry curvature must then be computed as a whole for those two bands. This is performed following the non-Abelian Berry connection generalization [21,34], resulting in valley Chern numbers of $+0.076$ and -0.076.

APPENDIX B: COMSOL SIMULATIONS

Numerical simulations were realized using the finite-element software COMSOL MULTIPHYSICS. A typical setup is presented in Fig. 10. The simulation domain, in light gray, comprises the resonator together with the input and output waveguides, emphasized with red lines. Note that the topological photonic crystal extends within the PMLs surrounding the physical domain; this configuration has been tested and chosen because it leads to weak backreflection. Perfectly matched layers have been set to Cartesian, except for the two tilted ones where the direction of attenuation has to be set by hand. The source is a rotating dipole localized at the center of one of the large holes of the topological waveguide. The transmission is evaluated by integrating the Poynting vector flow across the red line perpendicular to the output waveguide, whose length is long enough to capture all the power carried by the transmitted edge mode. The normalized transmission T is then obtained after normalization of the transmission by the power flowing along a straight waveguide without a resonator, computed in a similar way. Additionally, $1 - R$, where R is the normalized reflection, is computed with the same method but by integration along the red line perpendicular to the input waveguide.
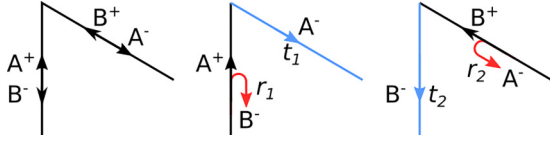
FIG. 11. Definition of the wave amplitudes and coupling coefficients for a corner.

APPENDIX C: SEMIANALYTICAL MODEL OF COUPLING MATRICES

We derive in this Appendix the analytical expressions of the scattering matrices between incoming and outgoing topological edge modes at either the corner of the linear waveguide (two inputs and two outputs) or a splitter (four inputs and four outputs). The calculation is based on energy conservation, time-reversal invariance, and mirror symmetry of the configuration.

1. Scattering matrix of a corner

A simple corner, in the most general situation, behaves like a coupler between one of the two incident edge modes A^+ and B^+ with the corresponding transmitted and reflected modes A^- and B^- (see Fig. 11). The process is linear and obeys the following relation:

$$\begin{bmatrix} A^- \\ B^- \end{bmatrix} = \mathbf{M}_C \begin{bmatrix} A^+ \\ B^+ \end{bmatrix} = \begin{bmatrix} t_1 & r_2 \\ r_1 & t_2 \end{bmatrix} \begin{bmatrix} A^+ \\ B^+ \end{bmatrix}.$$

Energy conservation implies that

$$|A^-|^2 + |B^-|^2 = |A^+|^2 + |B^+|^2, \quad \forall A^+, B^+.$$

The matrix $\mathbf{M}_C$ is then unitary:

$$\mathbf{M}_C^\dagger \mathbf{M}_C = \mathbf{1}.$$

Additionally, time-reversal symmetry implies that

$$\begin{bmatrix} B^+ \\ A^+ \end{bmatrix}^* = \mathbf{M}_C \begin{bmatrix} B^- \\ A^- \end{bmatrix}^* \Leftrightarrow \mathbf{S}_C \begin{bmatrix} A^+ \\ B^+ \end{bmatrix}^*$$

$$= \mathbf{M}_C \mathbf{S}_C \begin{bmatrix} A^- \\ B^- \end{bmatrix}^* \quad \text{with } \mathbf{S}_C = \begin{bmatrix} 0 & 1 \\ 1 & 0 \end{bmatrix},$$

which, combined with unitarity, implies $\mathbf{M}_C = \mathbf{S}_C \mathbf{M}_C^T \mathbf{S}_C$, and $t_1 = t_2$:

$$\mathbf{M}_C = \begin{bmatrix} t & r_1 \\ r_2 & t \end{bmatrix}.$$

The unitarity condition imposes

$$|r_1|^2 + |t|^2 = 1, \tag{C1a}$$
$$|r_2|^2 + |t|^2 = 1, \tag{C1b}$$
$$r_1 t^* + t r_2^* = 0. \tag{C1c}$$

Equations (C1a) and (C1b) impose $|r_1| = |r_2| = R$. Let us write $t = T \exp(i\tau)$, $r_1 = R \exp(i\rho_1)$, and $r_2 = R \exp(i\rho_2)$.

We have $R^2 + T^2 = 1$ and

$$RT(e^{i(\rho_1 - \tau)} + e^{i(\tau - \rho_2)}) = 0 \Longrightarrow \rho_1 - \tau$$
$$= \tau - \rho_2 + \pi + m2\pi, \quad m \in \mathbb{Z}$$

or

$$\rho_1 - \tau - \pi/2 + \rho_2 - \tau - \pi/2 + m2\pi = 0.$$

Writing

$$r_1 = R \exp[i(\rho_1 - \tau - \pi/2 + \tau + \pi/2)],$$
$$r_2 = R \exp[i(\rho_2 - \tau - \pi/2 + \tau + \pi/2)]$$
$$= R \exp\{i[-(\rho_1 - \tau - \pi/2) + \tau + \pi/2]\},$$

we pose $\rho = \rho_1 - \tau - \pi/2$ and we obtain $r_1 = iR \exp[i(\rho + \tau)]$ and $r_2 = iR \exp[i(-\rho + \tau)]$. Finally, the $\mathbf{M}_C$ matrix reads

$$\mathbf{M}_C = e^{i\tau} \begin{bmatrix} \cos\sigma & i\sin\sigma\, e^{i\rho} \\ i\sin\sigma\, e^{-i\rho} & \cos\sigma \end{bmatrix}, \tag{C2}$$

where we have introduced the angle σ such that $T = \cos\sigma$ and $R = \sin\sigma$. We end up with three degrees of freedom. Note that the eigenvalues of $\mathbf{M}_C$ are $\lambda^\pm = \exp[i(\tau \pm \sigma)]$.

Assuming symmetry of the junction, we can as well impose $r_1 = r_2 \Rightarrow \rho = 0$, and, with $\sigma \in [0, \pi]$ such as $R = \sin\sigma$ and $T = \cos\sigma$,

$$\mathbf{M}_C = e^{i\tau} \begin{bmatrix} \cos\sigma & i\sin\sigma \\ i\sin\sigma & \cos\sigma \end{bmatrix}.$$

For perfect topological protection, $\sigma = 0$ and $\mathbf{M}_C$ is diagonal.

2. Scattering matrix of a splitter

Let us consider now the splitter. Following Fig. 12, four outputs $\mathbf{X}^+ = [A^+, B^+, C^+, D^+]^T$ are now connected to four inputs $\mathbf{X}^- = [A^-, B^-, C^-, D^-]^T$. We must then extend the 2×2 to a 4×4 matrix with the following shape:

$$\mathbf{X}^- = \mathbf{M}_S \mathbf{X}^+ \Leftrightarrow \begin{bmatrix} A^- \\ B^- \\ C^- \\ D^- \end{bmatrix} = \begin{bmatrix} r_1 & \epsilon_2 & \epsilon_3' & t_4 \\ \epsilon_1 & r_2 & t_3 & \epsilon_4' \\ \epsilon_1' & t_2 & r_3 & \epsilon_4 \\ t_1 & \epsilon_2' & \epsilon_3 & r_4 \end{bmatrix} \begin{bmatrix} A^+ \\ B^+ \\ C^+ \\ D^+ \end{bmatrix}.$$

The mirror-symmetry of the corner, with respect to the dashed line in Fig. 12, leads to $\alpha_1 = \alpha_2$ and $\alpha_3 = \alpha_4$, where $\alpha = r, t, \epsilon, \epsilon'$. Additionally, time-reversal symmetry imposes

$$\begin{bmatrix} C^+ \\ D^+ \\ A^+ \\ B^+ \end{bmatrix}^* = \mathbf{M}_S \begin{bmatrix} C^- \\ D^- \\ A^- \\ B^- \end{bmatrix}^* \Leftrightarrow \mathbf{S}_S(\mathbf{X}^+)^* = \mathbf{M}_S \mathbf{S}_S(\mathbf{X}^-)^*,$$

$$\mathbf{S}_S = \begin{bmatrix} 0 & 0 & 1 & 0 \\ 0 & 0 & 0 & 1 \\ 1 & 0 & 0 & 0 \\ 0 & 1 & 0 & 0 \end{bmatrix}.$$

Combined with the unitarity of $\mathbf{M}_S$, the last relation leads to

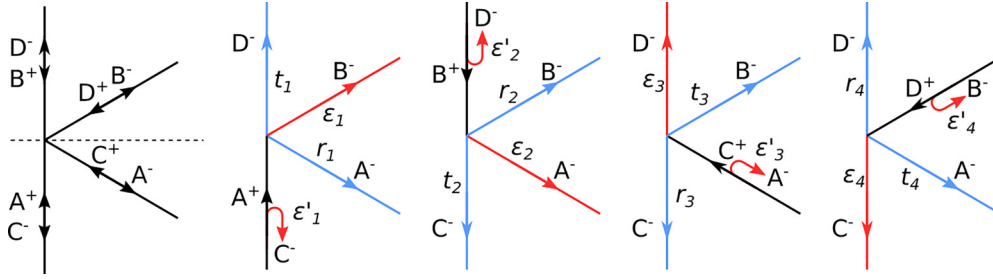$$\mathbf{M}_S = \mathbf{S}_S \mathbf{M}_S^T \mathbf{S}_S.$$

FIG. 12. Definition of the wave amplitudes and coupling coefficients for a splitter.

By comparison of both members of that equation, we finally see that $r_1 = r_2 = r_3 = r_4$ and $\epsilon_1 = \epsilon_2 = \epsilon_3 = \epsilon_4$. The matrix $\mathbf{M}_S$ can then be expressed in the following form:

$$\mathbf{M}_S = \begin{bmatrix} r & \epsilon & \epsilon'' & t' \\ \epsilon & r & t' & \epsilon'' \\ \epsilon' & t & r & \epsilon \\ t & \epsilon' & \epsilon & r \end{bmatrix}.$$

As $\mathbf{M}_S$ is unitary, it has four eigenvalues with unit modulus. We can exploit this property in order to find the full parametrization of the matrix. For that, we notice that the eigenvectors must be either symmetric or antisymmetric with respect to the line of symmetry of the splitter (dotted line in Fig. 12).

A set of symmetric vectors is $\mathbf{A}_1 = [1, 1, 0, 0]^T$ and $\mathbf{A}_2 = [0, 0, 1, 1]^T$, in which basis the matrix $\mathbf{M}_S$ reduces to

$$\mathbf{M}_S^A = \begin{bmatrix} r+\epsilon & t'+\epsilon'' \\ t+\epsilon' & r+\epsilon \end{bmatrix}.$$

As this matrix is unitary, it has the form given by Eq. (C2) and

$$r+\epsilon = \cos\phi e^{i\alpha}, \quad t'+\epsilon'' = i\sin\phi e^{i(\alpha+\beta)},$$
$$t+\epsilon' = i\sin\phi e^{i(\alpha-\beta)}.$$

Similarly, a set of antisymmetric vectors is $\mathbf{B}_1 = [1, -1, 0, 0]^T$ and $\mathbf{B}_2 = [0, 0, -1, 1]^T$, in which basis the matrix $\mathbf{M}_S$ reduces to

$$\mathbf{M}_S^B = \begin{bmatrix} r-\epsilon & t'-\epsilon'' \\ t-\epsilon' & r-\epsilon \end{bmatrix},$$

which leads to

$$r-\epsilon = \cos\phi' e^{i\alpha'}, \quad t'-\epsilon'' = i\sin\phi' e^{i(\alpha'+\beta')},$$
$$t-\epsilon' = i\sin\phi' e^{i(\alpha'-\beta')}.$$

Finally, we obtain

$$r = \frac{1}{2}(c_\phi e^{i\alpha} + c_{\phi'} e^{i\alpha'}), \quad \epsilon = \frac{1}{2}(c_\phi e^{i\alpha} - c_{\phi'} e^{i\alpha'}),$$
$$t' = \frac{i}{2}(s_\phi e^{i(\alpha+\beta)} + s_{\phi'} e^{i(\alpha'+\beta')}),$$
$$\epsilon'' = \frac{i}{2}(s_\phi e^{i(\alpha+\beta)} - s_{\phi'} e^{i(\alpha'+\beta')}),$$
$$t = \frac{i}{2}(s_\phi e^{i(\alpha-\beta)} + s_{\phi'} e^{i(\alpha'-\beta')}),$$
$$\epsilon' = \frac{i}{2}(s_\phi e^{i(\alpha-\beta)} - s_{\phi'} e^{i(\alpha'-\beta')}),$$

with $c_\phi = \cos\phi$, $c_{\phi'} = \cos\phi'$, $s_\phi = \sin\phi$, and $s_{\phi'} = \sin\phi'$. After some change of notation, we obtain

$$\mathbf{M}_S = \frac{e^{i\alpha}}{2} \begin{bmatrix} c_\phi e^{i\rho} + c_{\phi'} e^{-i\rho} & c_\phi e^{i\rho} - c_{\phi'} e^{-i\rho} & i(s_\phi e^{-i\delta} - s_{\phi'} e^{i\delta})e^{-i\beta} & i(s_\phi e^{-i\delta} + s_{\phi'} e^{i\delta})e^{-i\beta} \\ c_\phi e^{i\rho} - c_{\phi'} e^{-i\rho} & c_\phi e^{i\rho} + c_{\phi'} e^{-i\rho} & i(s_\phi e^{-i\delta} + s_{\phi'} e^{i\delta})e^{-i\beta} & i(s_\phi e^{-i\delta} - s_{\phi'} e^{i\delta})e^{-i\beta} \\ i(s_\phi e^{-i\gamma} - s_{\phi'} e^{i\gamma})e^{i\beta} & i(s_\phi e^{-i\gamma} + s_{\phi'} e^{i\gamma})e^{i\beta} & c_\phi e^{i\rho} + c_{\phi'} e^{-i\rho} & c_\phi e^{i\rho} - c_{\phi'} e^{-i\rho} \\ i(s_\phi e^{-i\gamma} + s_{\phi'} e^{i\gamma})e^{i\beta} & i(s_\phi e^{-i\gamma} - s_{\phi'} e^{i\gamma})e^{i\beta} & c_\phi e^{i\rho} - c_{\phi'} e^{-i\rho} & c_\phi e^{i\rho} + c_{\phi'} e^{-i\rho} \end{bmatrix}, \quad \text{(C3)}$$

with $\rho = -(\gamma + \delta)/2$. There are then six degrees of freedom.

If the topological protection is perfect ($\epsilon = \epsilon' = \epsilon'' = 0$), we have $\phi' = \phi$ and $\gamma = \delta = \rho = 0$, which gives

$$\mathbf{M}_S^0 = e^{i\alpha} \begin{bmatrix} \cos\phi & 0 & 0 & i\sin\phi e^{-i\beta} \\ 0 & \cos\phi & i\sin\phi e^{-i\beta} & 0 \\ 0 & i\sin\phi e^{i\beta} & \cos\phi & 0 \\ i\sin\phi e^{i\beta} & 0 & 0 & \cos\phi \end{bmatrix}.$$

Finally, starting from the expressions of $\mathbf{M}_S^A$ and $\mathbf{M}_S^B$, we show easily that the four eigenvalues of $\mathbf{M}_S$

are

$$\lambda_A^\pm = e^{i(\alpha+\rho\pm\phi)},$$
$$\lambda_B^\pm = e^{i(\alpha+\rho\pm\phi')}.$$

APPENDIX D: ESTIMATION OF THE CORNER a AND b COEFFICIENTS

The transmission (b) and reflection (a) coefficients of a single corner have been estimated by comparing the component H_z of the magnetic field computed along either a straight [solid line in Fig. 13(a), left] or a curved [solid line in Fig. 13(a), right] topological edge, both lines starting just
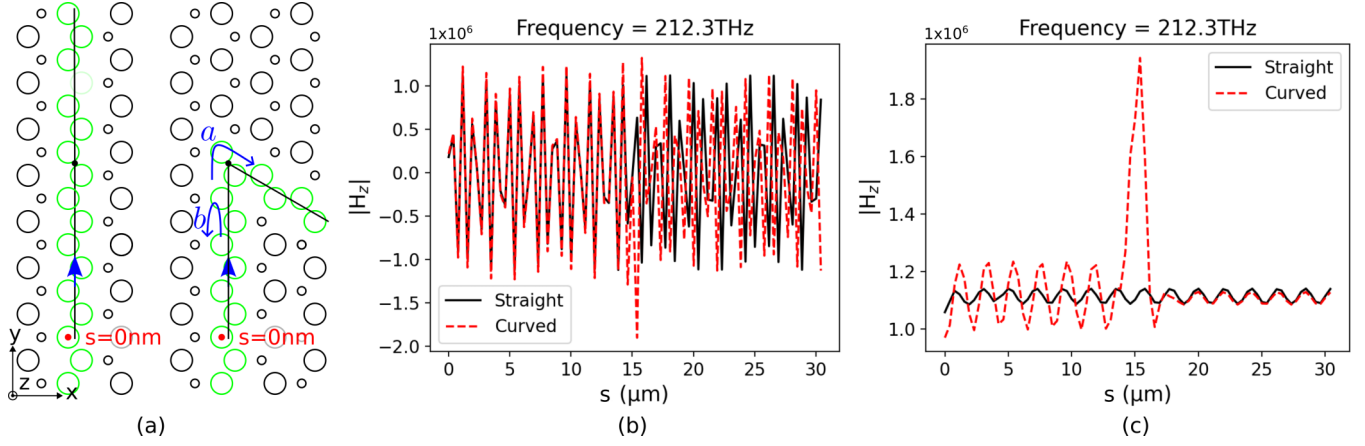
FIG. 13. (a) Straight (left) and curved (right) edges along which the z component of the magnetic field has been computed. (b) Real part of H_z along the straight (black solid line) or curved (red dashed line) path, as a function of the curvilinear position s measured from the position of the source (red dot). (c) Same as in (b) but for the amplitude of H_z.

beside the source (red dot). The real part and the amplitude of H_z are plotted in Figs. 13(b) and 13(c), respectively, for $F = 212.3$ THz.

The phase of the field after the corner in the curved waveguide differs by the transmission phase ϕ_a from the field propagating along the straight edge, as can be seen in Fig. 13(b). The phase ϕ_a can then simply be extracted from the complex value of H_z along the curved edge by comparison with the straight edge.

Concerning the amplitude of b, we can see in Fig. 13(c) that the reflection on the corner induces a noticeable amplitude modulation of the field before the corner ($s < 15$ μm). A smaller modulation is seen on the field propagating along the straight edge and the field transmitted though the corner, which is related to a small reflection on the PMLs. The superposition H_c of the incident and reflected fields with amplitude H_0 reads

$$H_c(y) = H_0\{\exp[ik(y - y_0)] + b\exp[-ik(y - y_0)]\}$$

$$\Rightarrow |H_c|(y) = |H_0|\sqrt{1 + |b|^2 + 2|b|\cos[2k(y - y_0) - \phi_b]},$$

where y_0 is the position of the corner and k the wave vector of the edge mode. We can verify that the contrast in amplitude is $|b|$. Numerically, the simulation data corresponding to Fig. 13(c) have been fitted using a function $f(y, r, s, t, u) = (r + s\sin ty + u)^{1/2}$, leading to

$$|b| = \frac{\sqrt{r+s} - \sqrt{r-s}}{\sqrt{r+s} + \sqrt{r-s}}.$$

As explained in the main text, the extracted coefficient contains the contribution from PMLs, which is the reason why the average value of $|b|$ on the frequency window has been retained. As ϕ_a and $|b|$ are known, the reflection and transmission coefficients are given, respectively, by

$$a = \sqrt{1 - |b|^2}\exp(i\phi_a),$$

$$b = i|b|\exp(i\phi_a).$$

APPENDIX E: SEMIANALYTICAL MODEL OF CAVITIES

We establish in this Appendix the matrix formalism used to model analytically the transmission across two types of triangular cavities. Both are excited by a waveguide linked to the cavity by a splitter, either directly at the tip [Fig. 14(a)] or at the edge [Fig. 14(b)]. Notice that the different segments between corners C and splitter S can have different lengths, even in the case of the tip-coupled cavity, due to the exact position of air holes forming the splitter. For those reasons, C-C and S-C lengths are written as L_0 and L_1, respectively, while in the edge-coupled cavity we need to introduce a third length L_2 (close to $L_0/2$) for the S-C segments.

In both cases, the incoupling field has the form

$$\mathbf{X}^+ = \begin{bmatrix} A^+ \\ B^+ \\ \mathbf{Y}^+ \end{bmatrix}, \quad A^+ = 1, \ B^+ = 0,$$

where $\mathbf{Y}^+$ contains the components of the input field inside the triangular cavity. We introduce as well a matrix $\mathbf{S}$ which

FIG. 14. Simplified description of (a) tip-coupled and (b) edge-coupled cavities in the semianalytical model. The waves crossing the splitters and corners are connected by scattering matrices at nodes and propagation phases along the segments.

selects the cavity components $\mathbf{Y}^+$,

$$\begin{bmatrix} 0 \\ 0 \\ \mathbf{Y}^+ \end{bmatrix} = \mathbf{SX}^+ \Rightarrow S_{ij} = \delta_{ij}(1 - \delta_{11})(1 - \delta_{22}),$$
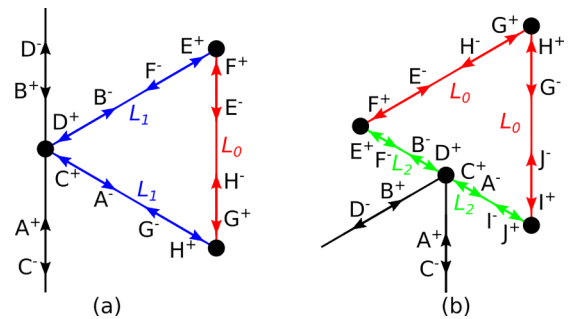
where δ_{ij} is the Kronecker symbol. We can then express

$$\mathbf{X}^+ = \mathbf{SX}^+ + \mathbf{X}^0, \quad \mathbf{X}^0 = [1, 0, \dots, 0]^T.$$

The two relations between $\mathbf{X}^+$ and $\mathbf{X}^-$ are

$$\mathbf{X}^- = \mathbf{CX}^+, \quad \mathbf{X}^+ = \mathbf{PX}^-.$$

The coupling matrix $\mathbf{C}$ is

$$\mathbf{C} = \begin{bmatrix} \mathbf{M}_S & & & 0 \\ & \mathbf{M}_C & & \\ & & \ddots & \\ 0 & & & \mathbf{M}_C \end{bmatrix},$$

where there are as many $\mathbf{M}_C$ in the matrix as there are corners in the triangular cavity, not counting the splitter. Note that in the edge-connected cavity, the (t, ϵ') and (t', ϵ'') coefficients must be exchanged as compared to the tip-connected cavity. The matrix $\mathbf{P}$ describes the phase relations between the field components inside the cavity.

Finally, we end up solving the linear system of equations

$$\mathbf{X}^- = [\mathbf{1} - \mathbf{CSP}]^{-1}\mathbf{CX}^0, \tag{E1}$$

from which we extract the transmission and reflection coefficients $T = |D^-|^2$ and $R = |C^-|^2$. For the tip-coupled cavity, we have the definitions [see Fig. 14(a)]

$$\mathbf{X}^\pm = [A^\pm \quad B^\pm \quad C^\pm \quad D^\pm \quad E^\pm \quad F^\pm \quad G^\pm \quad H^\pm]^T,$$

$$\mathbf{C} = \begin{bmatrix} \mathbf{M}_S & & 0 \\ & \mathbf{M}_C & \\ 0 & & \mathbf{M}_C \end{bmatrix},$$

$$\mathbf{P} = \begin{bmatrix} 0 & 0 & 0 & 1 & 0 & 0 & 0 & 0 \\ 0 & 0 & 1 & 0 & 0 & 0 & 0 & 0 \\ 0 & 0 & 0 & 0 & 0 & 0 & e^{i\phi_1} & 0 \\ 0 & 0 & 0 & 0 & 0 & e^{i\phi_1} & 0 & 0 \\ 0 & e^{i\phi_1} & 0 & 0 & 0 & 0 & 0 & 0 \\ 0 & 0 & 0 & 0 & 0 & 0 & 0 & e^{i\phi_0} \\ 0 & 0 & 0 & 0 & e^{i\phi_0} & 0 & 0 & 0 \\ e^{i\phi_1} & 0 & 0 & 0 & 0 & 0 & 0 & 0 \end{bmatrix},$$

with $\phi_i = nk_0 L_i$, where n is the effective index of the edge mode and $k_0 = 2\pi F/c$, with F the frequency of the wave and c the speed of light in vacuum. For the edge-coupled cavity [see Fig. 14(b)]

$$\mathbf{X}^\pm = [A^\pm \quad B^\pm \quad C^\pm \quad D^\pm \quad E^\pm \quad F^\pm \quad G^\pm \quad H^\pm \quad I^\pm \quad J^\pm]^T,$$

$$\mathbf{C} = \begin{bmatrix} \mathbf{M}'_S & & 0 & \\ & \mathbf{M}_C & & 0 \\ 0 & & \mathbf{M}_C & \\ & 0 & & \mathbf{M}_C \end{bmatrix},$$

$$\mathbf{P} = \begin{bmatrix} 0 & 0 & 0 & 1 & 0 & 0 & 0 & 0 & 0 & 0 \\ 0 & 0 & 1 & 0 & 0 & 0 & 0 & 0 & 0 & 0 \\ 0 & 0 & 0 & 0 & 0 & 0 & 0 & 0 & e^{i\phi_2} & 0 \\ 0 & 0 & 0 & 0 & 0 & e^{i\phi_2} & 0 & 0 & 0 & 0 \\ 0 & e^{i\phi_2} & 0 & 0 & 0 & 0 & 0 & 0 & 0 & 0 \\ 0 & 0 & 0 & 0 & 0 & 0 & 0 & e^{i\phi_0} & 0 & 0 \\ 0 & 0 & 0 & 0 & e^{i\phi_0} & 0 & 0 & 0 & 0 & 0 \\ 0 & 0 & 0 & 0 & 0 & 0 & 0 & 0 & 0 & e^{i\phi_0} \\ 0 & 0 & 0 & 0 & 0 & 0 & e^{i\phi_0} & 0 & 0 & 0 \\ e^{i\phi_2} & 0 & 0 & 0 & 0 & 0 & 0 & 0 & 0 & 0 \end{bmatrix},$$

where $\mathbf{M}'_S$ has the same expression as $\mathbf{M}_S$ but γ and δ have been exchanged and β has been changed into $-\beta$.

[1] A. B. Khanikaev, S. Hossein Mousavi, W.-K. Tse, M. Kargarian, A. H. MacDonald, and G. Shvets, Nat. Mater. **12**, 233 (2013).

[2] T. Ozawa, H. M. Price, A. Amo, N. Goldman, M. Hafezi, L. Lu, M. C. Rechtsman, D. Schuster, J. Simon, O. Zilberberg, and I. Carusotto, Rev. Mod. Phys. **91**, 015006 (2019).

[3] M. Segev and M. A. Bandres, Nanophotonics **10**, 425 (2020).

[4] S. Iwamoto, Y. Ota, and Y. Arakawa, Opt. Mater. Express **11**, 319 (2021).

[5] H. Price, Y. Chong, A. Khanikaev, H. Schomerus, L. J. Maczewsky, M. Kremer, M. Heinrich, A. Szameit, O. Zilberberg, Y. Yang, B. Zhang, A. Alú, R. Thomale, I. Carusotto, P. St-Jean, A. Amo, A. Dutt, L. Yuan, S. Fan, X. Yin *et al.*, J. Phys.: Photon. **4**, 032501 (2022).

[6] S. Barik, A. Karasahin, C. Flower, T. Cai, H. Miyake, W. DeGottardi, M. Hafezi, and E. Waks, Science **359**, 666 (2018).

[7] M. I. Shalaev, W. Walasik, A. Tsukernik, Y. Xu, and N. M. Litchinitser, Nat. Nanotechnol. **14**, 31 (2019).

[8] X.-T. He, E.-T. Liang, J.-J. Yuan, H.-Y. Qiu, X.-D. Chen, F.-L. Zhao, and J.-W. Dong, Nat. Commun. **10**, 872 (2019).

[9] N. Parappurath, F. Alpeggiani, L. Kuipers, and E. Verhagen, Sci. Adv. **6**, eaaw4137 (2020).

[10] S. Arora, T. Bauer, N. Parappurath, R. Barczyk, E. Verhagen, and L. Kuipers, Phys. Rev. Lett. **128**, 203903 (2022).

[11] R. Barczyk, N. Parappurath, S. Arora, T. Bauer, L. Kuipers, and E. Verhagen, Laser Photon. Rev. **16**, 2200071 (2022).

[12] A. Kumar, M. Gupta, P. Pitchappa, N. Wang, P. Szriftgiser, G. Ducournau, and R. Singh, Nat. Commun. **13**, 5404 (2022).

[13] L.-H. Wu and X. Hu, Phys. Rev. Lett. **114**, 223901 (2015).

[14] T. Ma and G. Shvets, New J. Phys. **18**, 025012 (2016).

[15] J. Noh, S. Huang, K. P. Chen, and M. C. Rechtsman, Phys. Rev. Lett. **120**, 063902 (2018).

[16] X. Wu, Y. Meng, J. Tian, Y. Huang, H. Xiang, D. Han, and W. Wen, Nat. Commun. **8**, 1304 (2017).

[17] J. Ma, X. Xi, and X. Sun, Laser Photon. Rev. **13**, 1900087 (2019).

[18] S. Arora, T. Bauer, R. Barczyk, E. Verhagen, and L. Kuipers, Light Sci. Appl. **10**, 9 (2021).

[19] Z. Wang, Y. Chong, J. D. Joannopoulos, and M. Soljačić, Nature (London) **461**, 772 (2009).

[20] B. Bahari, A. Ndao, F. Vallini, A. El Amili, Y. Fainman, and B. Kanté, Science **358**, 636 (2017).

[21] M. Blanco de Paz, C. Devescovi, G. Giedke, J. J. Saenz, M. G. Vergniory, B. Bradlyn, D. Bercioux, and A. García-Etxarri, Adv. Quantum Technol. **3**, 1900117 (2020).

[22] H. Xue, Y. Yang, and B. Zhang, Adv. Photon. Res. **2**, 2100013 (2021).

[23] K. Qian, D. J. Apigo, C. Prodan, Y. Barlas, and E. Prodan, Phys. Rev. B **98**, 155138 (2018).

[24] M. Saba, S. Wong, M. Elman, S. S. Oh, and O. Hess, Phys. Rev. B **101**, 054307 (2020).

[25] G. Arregui, J. Gomis-Bresco, C. M. Sotomayor-Torres, and P. D. Garcia, Phys. Rev. Lett. **126**, 027403 (2021).

[26] C. A. Rosiek, G. Arregui, A. Vladimirova, M. Albrechtsen, B. Vosoughi Lahijani, R. E. Christiansen, and S. Stobbe, Nat. Photon. **17**, 386 (2023).

[27] G. Siroki, P. A. Huidobro, and V. Giannini, Phys. Rev. B **96**, 041408(R) (2017).

[28] S. Barik, A. Karasahin, S. Mittal, E. Waks, and M. Hafezi, Phys. Rev. B **101**, 205303 (2020).

[29] M. J. Mehrabad, A. P. Foster, R. Dost, E. Clarke, P. K. Patil, A. M. Fox, M. S. Skolnick, and L. R. Wilson, Optica **7**, 1690 (2020).

[30] K. M. Devi, S. Jana, and D. R. Chowdhury, Opt. Mater. Express **11**, 2445 (2021).

[31] Z. Zhang, M. Dainese, L. Wosinski, and M. Qiu, Opt. Express **16**, 4621 (2008).

[32] S. Wong, M. Saba, O. Hess, and S. S. Oh, Phys. Rev. Res. **2**, 012011(R) (2020).

[33] J. Zhu, S. K. Ozdemir, Y.-F. Xiao, L. Li, L. He, D.-R. Chen, and L. Yang, Nat. Photon. **4**, 46 (2010).

[34] D. Vanderbilt, *Berry Phases in Electronic Structure Theory: Electric Polarization, Orbital Magnetization and Topological Insulators* (Cambridge University Press, Cambridge, 2018).